Revisiting the drag reduction problem using adjoint-based distributed forcing of laminar and turbulent flows over a circular cylinder

Philippe Meliga, Edouard Boujo, Marcello Meldi, François Gallaire

Accepted Manuscript

Revisiting the drag reduction problem using adjoint-based distributed forcing of laminar and turbulent flows over a circular cylinder

P. Meliga, E. Boujo, M. Meldi, F. Gallaire

PII: S0997-7546(17)30613-1
DOI: https://doi.org/10.1016/j.euromechflu.2018.03.009
Reference: EJMFLU 3274

To appear in: *European Journal of Mechanics / B Fluids*

Received date : 3 November 2017
Revised date : 4 March 2018
Accepted date : 20 March 2018

Please cite this article as: P. Meliga, E. Boujo, M. Meldi, F. Gallaire, Revisiting the drag reduction problem using adjoint-based distributed forcing of laminar and turbulent flows over a circular cylinder, *European Journal of Mechanics / B Fluids* (2018), https://doi.org/10.1016/j.euromechflu.2018.03.009

Revisiting the drag reduction problem using adjoint-based distributed forcing of laminar and turbulent flows over a circular cylinder

P. Meliga[a,*], E. Boujo[b], M. Meldi[c], F. Gallaire[d]

[a] *Aix-Marseille Univ., CNRS, Centrale Marseille, M2P2, Marseille, France*
[b] *CAPS, ETH Zurich, Zurich, Switzerland*
[c] *Université de Poitiers, CNRS, ISAE-ENSMA, Institut PPrime UPR 3346, 86962, Poitiers, France*
[d] *LFMI École Polytechnique Fédérale de Lausanne, Lausanne, Switzerland*

Abstract

This study assesses the ability of a sensitivity-based, span-wise homogeneous control velocity distributed at the surface of a circular cylinder to cut down the cost of reducing drag by more classical techniques, e.g., base bleed and lateral suction. At Reynolds number $Re = 100$, achieving the linear optimal reduction requires a time-dependent control velocity, set at each time instant against the sensitivity of the instantaneous drag. This approach however fails against even small control amplitudes because the system does not have time to adjust to the rapid change in the value of the wall velocity, and drag essentially increases. An efficient (albeit linearly suboptimal) reduction is however achieved using a steady control velocity set against the time averaged sensitivity. By doing so, drag decreases monotonically with the control momentum coefficient, and the sensitivity-based design exhibits a significant advantage over base bleed and lateral suction, that both reduce drag to a far lesser extent. Similar results are reported using various levels of modeling to compute approximations to the exact, time averaged sensitivity. The mean flow approach, that requires knowledge of the sole time averaged cylinder flow, yields especially promising results given the marginal computational effort. This approach is thus extended to the turbulent case at $Re = 3900$, where it achieves similar efficiency in the frame of both 2-D and 3-D RANS modeling. The study concludes with a discussion about the feasibility to extend the scope to span-wise periodic

*Corresponding author
Email address: philippe.meliga[@]univ-amu.fr (P. Meliga)

forcing velocities, following the line of thought of Kim & Choi [Phys. Fluids 17, 033103 (2005)].

Keywords: Flow control; drag reduction; numerical gradients; adjoint method; base bleed; lateral suction.

1. Introduction

Flow control, defined as the ability to modify flows to achieve a desired effect, is a field of considerable importance, that has been blooming in the last decades. In applications such as ocean shipping or airline traffic, reducing the overall drag by just a few percent while maintaining buoyancy or lift could help reducing fossil fuel consumption and CO_2 emission. A considerable amount of research has thus been devoted to control the flow over bluff bodies, well-known to exhibit unsteady vortex shedding and to produce a significant magnitude of drag.

Flow control for drag minimization has often been benchmarked in bluff body wakes, like the canonical circular and square cylinder flows. A wide variety of flow control strategies have been developed over the years : in addition to open-loop methods featuring either passive appendices (e.g., end plate, splitter plate, small secondary cylinder, or flexible tail) or actuating devices (e.g., plasma actuation, steady or unsteady base bleeding, rotation), closed-loop strategies have also been implemented (e.g. via transverse motion, blowing/suction, rotation, all relying on an appropriate sensing of flow variables). An overview of the recent achievements and perspectives can be found in several comprehensive surveys; see, e.g., Refs. [1–9], and the references therein. Nonetheless, many of the proposed control strategies are based on a trial and error approach, and therefore require extensive and costly experimental or numerical campaigns. In parallel, optimal control strategies, relying on a rigorous optimization mathematical formalism, have also been developed to achieve an optimal design with minimal effort. These methods proceed from so-called sensitivity techniques, and feature the efficient computation of the objective gradient with respect to the control variable through an adjoint formulation [10–16].

While optimal control methods apply easily to steady flows, they are increasingly difficult to apply rigorously as the Reynolds numbers increase and

unsteadiness and turbulence set in. In this paper, we thus consider various approximations of optimal control design strategies relying on a span-wise homogeneous control velocity distributed at the surface of a circular cylinder to efficiently reduce drag. In Secs. 3 and 4, we consider a Reynolds number $Re = 100$ for which the flow is 2-D and time periodic. We proceed to show that the steady control velocity obtained from the optimal analysis of the time-averaged, mean flow performs more robustly than the time-dependent control velocity obtained from the optimal analysis of the instantaneous flow. We also show that drag is efficiently reduced using approximations of the steady control velocity, obtained either from a self-consistent analysis, whose optimal encompasses the effect of the control on both the mean and the fluctuating components of the cylinder flow [17], or from a mean flow approach, whose solution takes into account the sole effect on the mean cylinder flow [16, 18]. Finally, we show that the optimal control approach allows cutting down the cost of reducing drag by classical blowing and suction techniques. In Sec. 5, we consider a turbulent case at the Reynolds number $Re = 3900$ and show that the mean flow approach (the only one that carries over for now without tremendous numerical and theoretical developments) achieves similar efficiency in the frame of both 2-D and 3-D RANS modeling. Preliminary results obtained by LES are also provided to assess the influence of the turbulence model. In Sec. 6, we finally discuss the present span-wise homogeneous control in the light of another approach used in the literature to control vortex shedding by span-wise periodic disturbances (the helical strake is a typical example [19], which reduces the force fluctuations but increases the mean drag). We compare especially our results to those of Kim and Choi [20], who report a successful mitigation of drag using span-wise periodic blowing and suction from slots located at upper and lower surfaces of the cylinder.

2. Problem formulation

We investigate the two-dimensional (2-D), incompressible flow past a span-wise infinite circular cylinder, forced open-loop by a 2-D, wall-normal velocity u_w^* distributed over the cylinder surface. We denote respectively by x and y the stream-wise and cross-wise directions of the Cartesian coordinate system, whose origin is at the cylinder center, and by $\mathbf{i}$ and $\mathbf{j}$ the related unit vectors. The

Reynolds number is $Re = u_\infty^* d^*/\nu^*$, with d^* the diameter of the cylinder, u_∞^* the free-stream velocity and ν^* the constant kinematic viscosity. The cylinder flow is denoted by $(\mathbf{u}, p)$, where $\mathbf{u}$ is the velocity vector and p is the pressure. The flow motion in space domain Ω is governed by the Navier–Stokes equations (NSE)

$$\partial_t \mathbf{u} + \mathbf{u} \cdot \boldsymbol{\nabla} \mathbf{u} - \boldsymbol{\nabla} \cdot \boldsymbol{\sigma}(p, \mathbf{u}) = \mathbf{0}\,, \qquad \mathbf{u}|_\Gamma = u_w \mathbf{n} = \mathbf{u}_w\,, \tag{1}$$

where the cylinder surface Γ has unit outward normal $\mathbf{n}$,

$$\boldsymbol{\sigma}(p, \mathbf{u}) = -p\mathbf{I} + Re^{-1}(\nabla \mathbf{u} + \nabla \mathbf{u}^T)\,, \tag{2}$$

is the linear stress tensor, and T is the transpose. We omit the continuity equation $\boldsymbol{\nabla} \cdot \mathbf{u} = 0$ to ease the reading, as it is understood that all velocity fields considered in the following are divergence free because of incompressibility.

In the following analysis, we use the L^2 space inner product for continuous real-valued functions on Γ defined by

$$(\mathbf{v} \,|\, \mathbf{w})_\Gamma = \frac{1}{2} \int_0^{2\pi} \mathbf{v}^T \mathbf{w} \, \mathrm{d}\theta\,, \tag{3}$$

where θ is the azimuthal position at the cylinder surface (measured from the rear stagnation point) and the associated space-time inner product defined by $(\!(\mathbf{v} \,|\, \mathbf{w})\!)_\Gamma = \overline{(\mathbf{v} \,|\, \mathbf{w})_\Gamma}$, where the overline indicates an average over time. The cylinder mean drag coefficient per unit length, simply termed mean drag (or even drag) to ease the reading, is thus

$$\overline{D} = 2(\!(\boldsymbol{\sigma}(p, \mathbf{u}) \cdot \mathbf{n} \,|\, \mathbf{i})\!)_\Gamma\,, \tag{4}$$

and we distinguish for clarity between the drag $\overline{D}_0$ of the uncontrolled cylinder flow, and that $\overline{D}_w$ of the controlled cylinder flow. The cost of the control is measured by the momentum coefficient

$$c_\mu = 2(\!(\mathbf{u}_w \,|\, \mathbf{u}_w)\!)_\Gamma\,, \tag{5}$$

physically representing the ratio (also per unit length) of the induced mean flux of momentum to a reference momentum built from the free stream dynamic pressure and the cylinder diameter [21]. The premise of this study is that the cost of reducing drag by classical blowing and suction techniques can be cut

down from knowledge of the drag sensitivity $\zeta(t,\theta)$, by definition such that

$$\delta\overline{D}_{w,lin} = (\!(\zeta \,|\, u_w)\!)_\Gamma \,, \tag{6}$$

where $\delta\overline{D}_{w,lin}$ is the linear estimate of the control-induced drag variation $\overline{D}_w - \overline{D}_0$. Note that the sensitivity itself needs to be computed only once at the cylinder wall since we force open loop.

We insist that the focus of the paper is not on how to derive the sensitivity by the adjoint method, which is a topic thoroughly covered in a series of recent papers [16–18] to which the interested reader is referred for further deepening. The line of thought is conversely to take the output sensitivity as a given, to set

$$u_w(t,\theta) = -\alpha\zeta(t,\theta) \,, \tag{7}$$

where α is a constant coefficient used to adjust the cost of the control ($\alpha > 0$ to move against the gradient), and to assess efficiency by direct numerical simulation (DNS). We mention all the same that the drag sensitivity is expressed after Refs. [16, 18] as

$$\zeta = [\boldsymbol{\sigma}(-p^\dagger, \mathbf{u}^\dagger)\cdot\mathbf{n}]\cdot\mathbf{n} \,, \tag{8}$$

where $(\mathbf{u}^\dagger, p^\dagger)$ is the time-dependent, adjoint cylinder flow, solution to

$$-\partial_t\mathbf{u}^\dagger + \mathbf{u}^\dagger\cdot\boldsymbol{\nabla}\mathbf{u}^T - \mathbf{u}\cdot\boldsymbol{\nabla}\mathbf{u}^\dagger - \boldsymbol{\nabla}\cdot\boldsymbol{\sigma}(-p^\dagger,\mathbf{u}^\dagger) = \mathbf{0}\,. \qquad \mathbf{u}^\dagger|_\Gamma = 2\mathbf{i}\,, \tag{9}$$

We shall not go into the technicalities of it (all details are available in Appendix C of Ref. [16] and Section 2 of Ref. [18]; see also the Appendix in Ref. [22]), but Eq. (8) proceeds from a variational technique based on the computation of Lagrange multipliers. Starting from the uncontrolled cylinder flow, i.e., the solution to Eq. (1) with $\mathbf{u}|_\Gamma = \mathbf{0}$, one considers the linear perturbation $(\delta\mathbf{u}, \delta p)$ induced by a small control velocity δu_w, as governed by the linearized Navier–Stokes equation with boundary condition $\delta\mathbf{u}|_\Gamma = \delta u_w\mathbf{n} = \delta\mathbf{u}_w$. Multiplying $\mathbf{u}^\dagger$ and $p^\dagger$ onto the linear momentum and continuity equations, using the divergence theorem to integrate by parts over Ω, and finally integrating in time over the span of the simulation[1], gives

$$(\!(\mathbf{u}^\dagger \,|\, \boldsymbol{\sigma}(\delta p, \delta\mathbf{u})\cdot\mathbf{n})\!)_\Gamma - (\!(\boldsymbol{\sigma}(-p^\dagger,\mathbf{u}^\dagger)\cdot\mathbf{n} \,|\, \delta\mathbf{u})\!)_\Gamma = 0\,, \tag{10}$$

[1] We use classical conditions $\delta\mathbf{u}(0) = \mathbf{u}^\dagger(T) = \mathbf{0}$ corresponding to a fixed initial cylinder flow and a zero initial adjoint cylinder flow.

Table 1: Details of the computational mesh used in the analysis at $Re = 100$. L_x and L_y are the dimensions of the domain in the stream-wise and cross-wise directions, respectively. n_θ is the number of grid points at the cylinder surface, n is the total number of grid points, and DoF is the number of degrees of freedom.

L_x	L_y	n_θ	n	DoF
[-30, 60]	[-25, 25]	320	5.4×10^4	3.8×10^5

Table 2: Mean drag coefficient ($\overline{D}_0$), r.m.s. lift coefficient (L'_0), and Strouhal number (St) of the uncontrolled cylinder flow at $Re = 100$, together with numerical data from the literature.

Contribution	$\overline{D}_0$	L'_0	St
Present	1.336	0.229	0.166
Reference[a]	$1.322 - 1.336$	$0.226 - 0.234$	0.164

a: data compiled from Refs. [20, 23, 24].

which is recast into

$$2(\!(\mathbf{i} \,|\, \boldsymbol{\sigma}(\delta p, \delta \mathbf{u}) \cdot \mathbf{n})\!)_\Gamma - (\!([\boldsymbol{\sigma}(-p^\dagger, \mathbf{u}^\dagger) \cdot \mathbf{n}] \cdot \mathbf{n} \,|\, \delta u_w)\!)_\Gamma = 0\,, \tag{11}$$

using the boundary conditions at the cylinder surface. Equation (8) then deduces straightforwardly from Eq. (6), as the left-hand side in Eq. (11) happens to be exactly the linear control-induced drag variation $\delta\overline{D}_{w,lin}$.

3. Time-dependent actuation at $Re = 100$

In the remainder of this section, the Reynolds number is set to $Re = 100$, for which both the cylinder flow and adjoint cylinder flow are time periodic [25]. All calculations are performed with the finite element solver presented and validated in Refs. [16, 26], that uses Mini elements (i.e., continuous piecewise affine functions) for space discretization and a second-order Crank–Nicholson scheme for time discretization. The set-up is identical to that in Ref. [17], for which a summary of the mesh information is given in Table 1. Numerical accuracy has been assessed by validating typical uncontrolled flow quantities (e.g., mean value of drag, root mean square value of lift, Strouhal number) against several reference studies, which yields the high level of compliance provided in Table 2.

It is a well known feature that time-dependent adjoint solutions must be computed by marching the governing equations backwards in time, which requires here knowledge of the entire history of the uncontrolled cylinder flow solution. All results presented in the following are obtained using the exact same approach as in Ref. [16], i.e., solving first Eq. (1), writing all time steps to disk, then solving Eq. (9) over the same time span and with the same time step $\Delta t = 0.05$. We consider only starting the control from a fully developed shedding to discard the late time steps of the adjoint simulation, where the early transient of the uncontrolled cylinder flow produces large, unphysical control velocities (actually, we discard also the early time steps corresponding to the transient of the adjoint solution to compute meaningful time averages of the sensitivity integrands). The so-obtained time periodic control velocity is illustrated in Fig. 1 at four time instants sampled over a vortex-shedding period. The first snapshot in Fig. 1(a) corresponds to a substantial suction distributed over the upper half of the cylinder surface, together with a blowing of lesser magnitude over the lower half. The third snapshot unveils the same pattern of substantial suction and lesser blowing, only both halves of the cylinder surface exchange roles because the phase is shifted by half a shedding period. The transition from one pattern to the other is accompanied by a distortion of the blowing velocity at the rear surface, found to be stronger on the half of the cylinder at which suction is applied, and by an almost constant blowing on the front surface.

Despite the effort gone into designing the control velocity from accurate sensitivity calculations, we show in Fig. 2(a) that the nonlinear value of $\overline{D}_w$ increases with c_μ. This is especially unexpected given that the linear, optimal value computed as

$$\overline{D}_{w,lin} = \overline{D}_0 + (\!(\zeta \,|\, u_w)\!)_\Gamma \,, \tag{12}$$

decreases rapidly, as the results reported as the fine solid line suggest that an amplitude as low as $c_\mu = 2 \times 10^{-4}$ should suffice to reduce drag by 5%. A closer look at the smallest values of c_μ in Fig. 2(b) unveils that the control does actually reduce drag while following the linear predictions, only the range of efficiency is extremely narrow since drag increases back past $c_\mu \sim 5 \times 10^{-6}$, at which point it has been reduced by a marginal 0.3%. Figure 2(c) further analyzes this singular behavior through the time evolution of the instantaneous

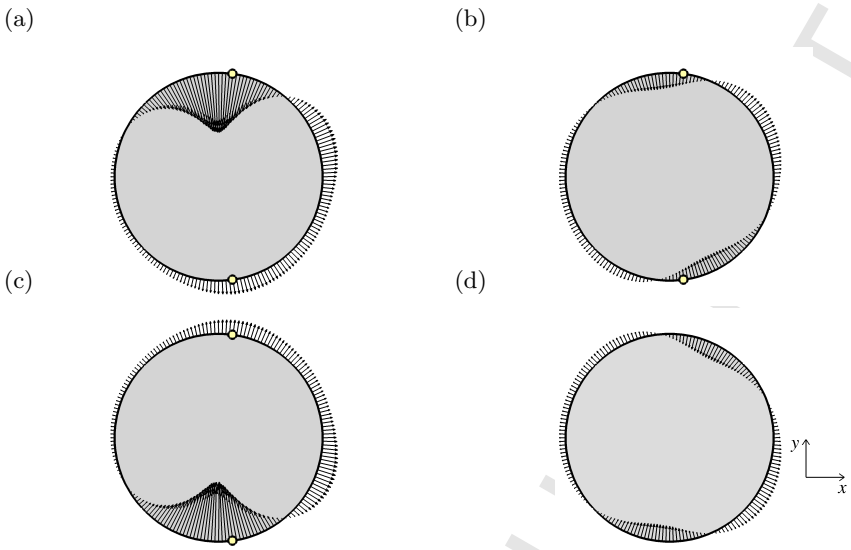

Figure 1: Time-dependent actuation: distribution of the wall velocity over a shedding period. (a) corresponds to maximum sucked velocity on the upper half of the cylinder surface, while (c)-(d) are successively shifted by a quarter of the shedding period. The yellow circles mark the position of the mean separation points - $Re = 100$.

drag. Since there is no loss of generality in doing so, we conveniently set the control to start at $t = 0$, using a value $c_\mu = 10^{-4}$ of the momentum coefficient that yields an overall increase of drag. We notice that drag decreases instantly, then starts to increase after 27 time units (approximately 4 shedding periods). This does not proceed from detrimental transient effects, as we obtain similar results by increasing linearly the aerodynamic coefficient from zero up to the desired value within a user-controlled time span τ, as achieved substituting

$$u_w(t,\theta) = -\alpha \left(1 + \frac{t}{\tau}\right) \zeta(t,\theta)\,, \tag{13}$$

for the control velocity in the range from $t = -\tau$ to 0, in a way such that the same value of c_μ (encompassing the extra cost of forcing at times $t < 0$) is achieved at $t = 0$. Beyond the expected difference in the initial reduction rate (the larger τ, the smaller the reduction rate), the effect is essentially on the time τ_i at which drag starts to increase, measured in Fig. 2(d) from $t = 0$ and found to decrease with τ. A negative value is reported for the largest value $\tau = 50$, meaning that drag even starts to increase *before* the aerodynamic coefficient has

reached its maximum value. Similar results have been obtained setting

$$u_w(t,\theta) = -\alpha\zeta(t-\tau_d,\theta)\,, \tag{14}$$

and varying the delay τ_d between the time instant at which the sensitivity is computed and the one at which the ensuing control velocity is applied at the cylinder surface (not shown here for conciseness). Note, this is not the classical shortcoming encountered applying linear optimal control distributions to fully nonlinear systems, i.e., the fact that the linear efficiency of the control is progressively, nonlinearly cushioned until it is no longer effective. It is rather an example of how a time-dependent, sensitivity-based control design can fail against even small actuation amplitudes because its tremendous linear efficiency ultimately generates a large nonlinearity. This may seem counter-intuitive at first, but despite the small values of c_μ at stake, the control-induced flow modification departs from its linear estimate because achieving the expected drag reduction imposes to substantially reorganize the near-wall pressure and velocity distributions at each time instant. The errors add up because the system does not have time to adjust to the rapid change in the value of the wall velocity, up to the point where the linear theory breaks down. Such results cannot be generalized, but instead must be assessed on a case-by-case basis. Still, they serve as a reminder that there are many pitfalls when seeking systematical quick-hit payoffs from the knowledge of numerical gradients, as we shall see in the following that restricting to steady, suboptimal, control velocities yields much more convincing results.

4. Steady actuation at $Re = 100$

In this section, the Reynolds number remains set to $Re = 100$, but we restrict from now on to time-independent, steady velocity distributions $u_w = u_w(\theta)$. Pulling the control velocity out of the time integral in Eq. (6) yields simply

$$\delta\overline{D}_{w,lin} = (\overline{\zeta}\,|\,u_w)_\Gamma\,, \tag{15}$$

where $\overline{\zeta}(\theta)$ is now a steady sensitivity distribution expressed from the mean adjoint cylinder flow $(\overline{\mathbf{u}}^\dagger, \overline{p}^\dagger)$ as

$$\overline{\zeta} = [\boldsymbol{\sigma}(-\overline{p}^\dagger, \overline{\mathbf{u}}^\dagger)\cdot\mathbf{n}]\cdot\mathbf{n}\,, \tag{16}$$

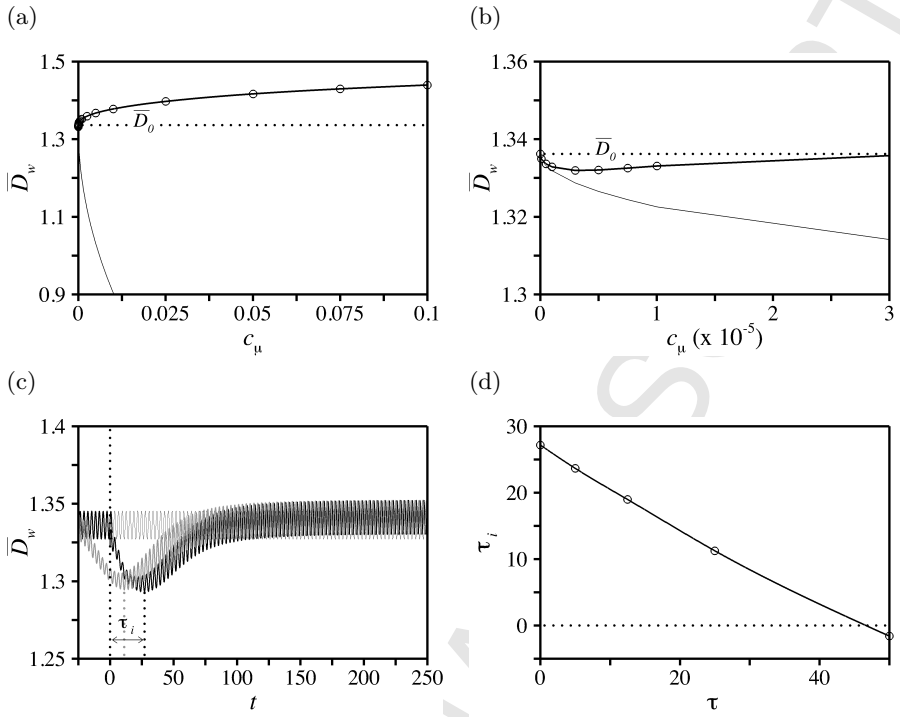

Figure 2: (a) Mean drag of the cylinder flow forced by a control velocity set against the time-dependent sensitivity, i.e., $u_w(t,\theta) = -\alpha\zeta(t,\theta)$. The solid and dashed lines correspond respectively to the nonlinear value drag computed by DNS, and to the open-loop, linear optimal value computed from Eq. (17) - $Re = 100$. (b) Close-up at small control amplitudes. (c) Time evolution of drag for a time-dependent control velocity set against the instantaneous sensitivity. The black line is obtained setting the aerodynamic momentum coefficient to $c_\mu = 10^{-4}$ at $t = 0$, as marked by the leftmost vertical dots. The grey line is obtained increasing linearly the coefficient from zero up to 10^{-4} within a time span $\tau = 25$, as defined by Eq. (13). The fine line denotes the drag of the uncontrolled cylinder flow - $Re = 100$. (d) Time τ_i after which drag starts to increase against time span τ used to increase linearly the momentum coefficient from zero.

since the stress tensor is linear in the flow variables. In the frame of the above time-stepping analysis, it is straightforward to compute the exact sensitivity by averaging over time the adjoint solution to Eq. (9), as in Refs. [16, 18]. This yields the control velocity shown in Fig. 3(a), that consists of a strong suction distributed over the lateral sides of the cylinder, together with a lower amplitude blowing at the front and rear surfaces.

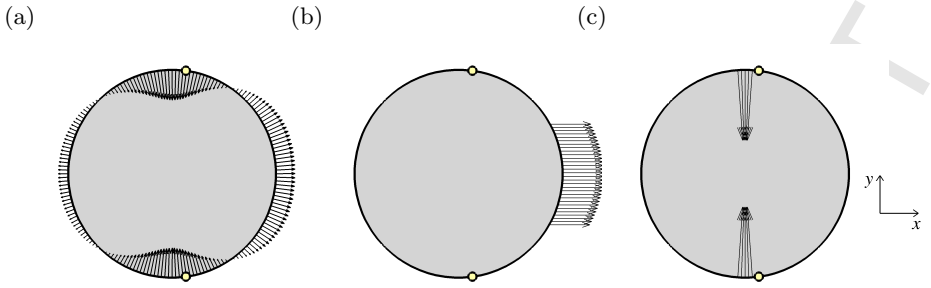

Figure 3: (a) Steady actuation: distribution of the wall velocity built from the exact, time averaged sensitivity function - $Re = 100$. (b,c) Same as (a) for (b) base bleed and (c) lateral suction. The size of the arrows has been adjusted for all distributions to give the same value of c_μ.

4.1. Exact sensitivity versus base bleed and lateral suction

We show in Fig. 4(a) that the sensitivity-based control velocity reduces monotonically D_w even for large values of the momentum coefficient c_μ. We also report typical time evolutions in Figs. 4(c) and 4(d) to unveil how quickly drag settles on its controlled value, as this takes ten or so shedding periods regardless of the control distribution (these results, as well as those reported in the following, are for a control starting from the fully developed shedding, but it has been checked that identical results are obtained if the control is conversely started from rest). Even better, the linear, optimal value computed as

$$\overline{D}_{w,lin} = \overline{D}_0 + (\overline{\zeta} \,|\, u_w)_\Gamma \,, \tag{17}$$

and shown as the fine black line provides a fair prediction of the achieved non-linear variation throughout the whole range of c_μ. This highlights the improved efficiency of steady, adjoint-based actuation over its time-dependent counterpart considered in Sec. 3, and proves feasible to design a reliable control at a reduced cost. Note that the intended reduction of the mean drag has been checked to be systematically accompanied by a mitigation of the drag and lift fluctuations, which is not obvious a priori because the sensitive regions (as well as the effect of a given forcing in these regions) are peculiar to each individual quantity[2]. Note also that if c_μ is so large as to make the flow stable and stationary (i.e.,

[2]The sensitivity analysis can be tailored to specifically reduce the r.m.s. values of drag and lift [16], but this lies out of the scope of the present study.

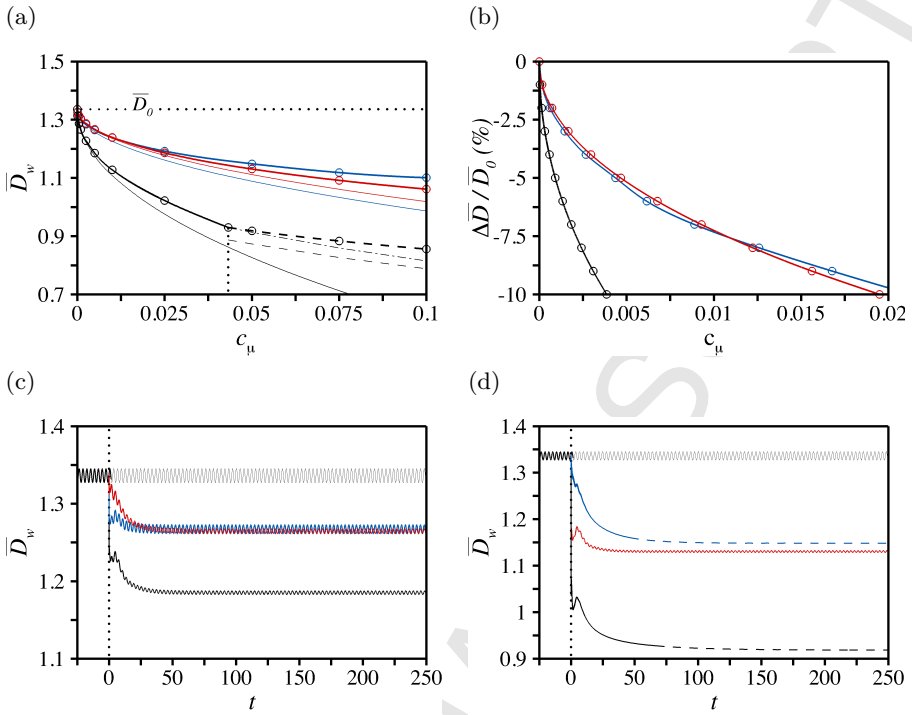

Figure 4: (a) Mean drag of the cylinder flow forced by a steady control velocity set against the time averaged sensitivity, computed from Eq. (16) by a time-stepping approach. The thick (resp. thin) black line is the nonlinear value of drag (resp. the linear optimal computed from Eq. (12)), and the solid (resp. dashed) pattern indicates time periodic (resp. steady) values. The thin dashed line (resp. dash-dotted line) is the linear value computed from the sensitivity of the steady, uncontrolled drag (resp. the steady value of the uncontrolled drag at $c_\mu = 0.0432$, as marked by the vertical dots). The results obtained using base bleed (resp. lateral suction) are reported in blue (resp. in red) - $Re = 100$. (b) Relative drag variation against c_μ. (c,d) Time evolution of drag for (c) $c_\mu = 0.005$, and (d) $c_\mu = 0.05$. The fine line is the drag of the uncontrolled cylinder flow.

it quenches completely the instability, which occurs here for $c_\mu = 0.0432$, as obtained by global, linear stability analysis of the controlled flow and evidenced in Fig. 4 by the dashed lines), it is the sensitivity of the steady drag, not that of the mean drag, that provides accurate predictions.

We also report the results obtained using two classical techniques :

- base bleed, i.e., blowing fluid into the wake through a small section of the rear cylinder surface; see, e.g. [27–29]. The present results (in blue in all related figures) pertain to a blowing parallel to the free stream, applied

through a rear slot covering the angular range $|\theta| \leq 15$ (in degrees).

- lateral suction, i.e., sucking fluid through sections located on either side of the cylinder surface, close to the mean separation points [20]. The present results (in red in all related figures) pertain to a sucking normal to the cylinder surface applied through slots covering the angular ranges $|\theta \pm 90| \leq 5$, i.e., just upstream of the mean separation points.

From a physical standpoint, the related distributions shown in Figs. 3(b) and 3 (c) are consistent with the main features of the sensitivity based-distribution, since fluid is either blown through the rear surface or sucked through the lateral surfaces. Base bleed and lateral suction however use only a small portion of the control surface and therefore require larger control velocities to achieve the same value of c_μ, as evidenced by the size of the corresponding arrows in Fig. 3. As shown in Fig. 4, this yields important differences in terms of control efficiency: while all three distributions end up reducing drag, the reduction achieved by sensitivity-based control is systematically and substantially larger. This is emphasized in Fig. 4(b) recasting the obtained results in terms of relative drag variations. Using base bleed or lateral suction, a momentum coefficient $c_\mu \simeq 0.020$ is needed to reduce drag by 10%, but a value as little as $c_\mu \simeq 0.004$ suffices with the sensitivity-based optimal control, hence a tremendous cut by approximately 80%. Note that linear sensitivity (dashed lines) predicts that lateral suction performs slightly less well than base bleed, but nonlinear results (solid lines) show that it performs better when the control amplitude is increased above $c_\mu \simeq 0.010$, which highlights the importance of nonlinear validation.

4.2. Application to pressure and viscous drag

The drag variations obtained with nonlinear simulations decompose into pressure and viscous contributions, that are of interest to analyze in more details the effect of the control, and also to compare with experimental measurements, where it is common that only one of the two contributions is available. It is thus proposed here to compute the sensitivities of each component as an attempt to optimize their individual reductions. This can be done with minor modifications to the adjoint-based framework, namely, the pressure drag sensitivity proceeds from the exact same adjoint equations, only the adjoint velocity at the cylinder

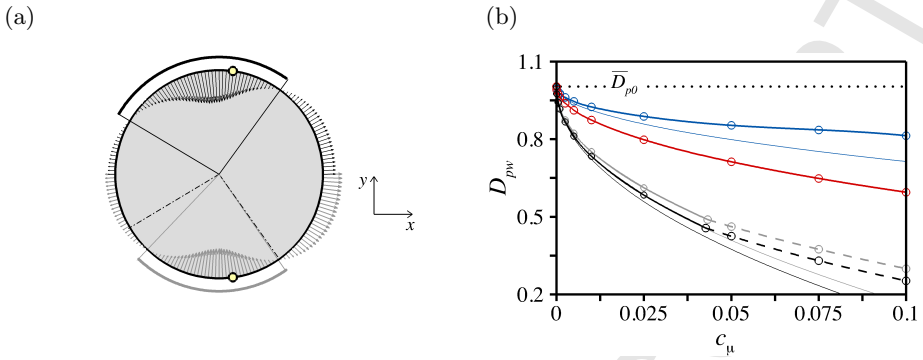

Figure 5: (a) Distribution of the wall velocity built from the pressure drag sensitivity (upper half, black arrows) and the total drag sensitivity (lower half, grey arrows). The arcs of a circle enhance the sections of the cylinder surface where the sensitivity is positive (black arc for the pressure, whose ends are reported in the lower half by the dash-dotted lines, and grey for the total drag, respectively). (b) Same as Fig. 4 for the mean pressure drag. The thick (resp. thin) grey line is the nonlinear (resp. linear) value obtained setting the control velocity against the sensitivity of the total drag.

surface is now given by

$$\mathbf{u}^\dagger|_\Gamma = 2(\mathbf{n}\cdot\mathbf{i})\mathbf{n}\,. \tag{18}$$

This is because the viscous wall stresses are purely tangential in the incompressible regime [30, 31], which yields

$$[\boldsymbol{\sigma}(p,\mathbf{u})\cdot\mathbf{n}]\mathbf{n} = -p\,, \tag{19}$$

and allows writing the mean pressure drag as

$$\overline{D}_p = (\!(\boldsymbol{\sigma}(p,\mathbf{u})\cdot\mathbf{n}\,|\,2(\mathbf{n}\cdot\mathbf{i})\mathbf{n})\!)_\Gamma\,. \tag{20}$$

The steady control velocity set against the time averaged pressure drag sensitivity is unveiled in the upper half in Fig. 5(a). Similar to the total drag sensitivity reproduced in the lower half, it features a suction distributed over the lateral sides and a blowing at the front and rear surfaces (again, the size of the arrows has been adjusted for both distributions to give the same value of c_μ). There are subtle differences in the sensitive regions, though, namely the pressure drag sensitivity is lower at the front and rear surfaces, but almost identical on the lateral sides, therefore its suction area is larger. This is evidenced by the arcs of a circle in Fig. 5(a), that mark the sections of the cylinder surface where

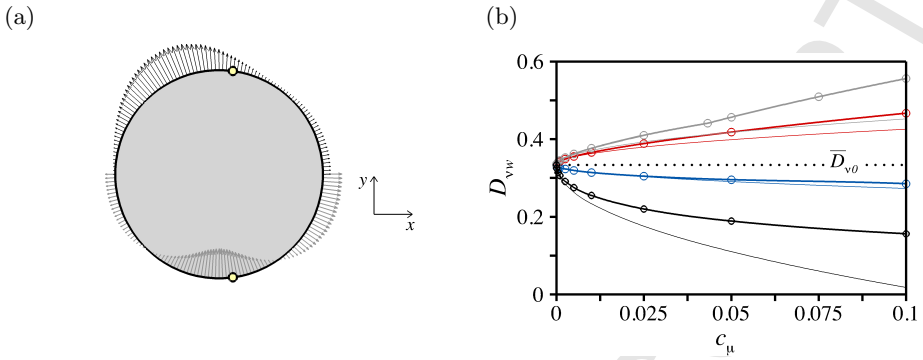

Figure 6: Same as Fig. 5 for the viscous drag.

the sensitivity is positive (black and grey arcs for the pressure and total drag, respectively). Nonetheless, the pressure and total drag are sensitive in the same regions and can thus be reduced using the same control distributions; see Fig. 5 (b) comparing the effect of a control velocity built from either the pressure drag sensitivity (in black) or the total drag sensitivity (in grey). The latter approach substantially reduces $\overline{D}_p$ although it is not specifically designed for it. The former approach however remains more effective linearly (which could have been expected since it is the linear optimal for the intended target) and nonlinearly, because it makes use of the aforementioned extended suction area. Anyhow, both distributions exhibit a significant advantage over base bleed and lateral suction, that both reduce the pressure drag to a far lesser extent.

By linearity, the sensitivity of the viscous drag $\overline{D}_\nu = \overline{D} - \overline{D}_p$ is obtained by solving the exact same adjoint equations, together with the adjoint forcing velocity

$$\mathbf{u}^\dagger|_\Gamma = 2\mathbf{i} - 2(\mathbf{n}\cdot\mathbf{i})\mathbf{n}\,. \tag{21}$$

The steady control velocity set against the time averaged viscous drag sensitivity is shown in the upper half in Fig. 6(a). It corresponds to a wall blowing, distributed upstream of the separation point and extending up to the front stagnation point, together with a weak blowing at the rear surface, and does allow reducing $\overline{D}_\nu$ linearly and nonlinearly; see the black lines in Fig. 6(b). In contrast, using the total drag sensitivity (in grey) does just the opposite, i.e., it increases $\overline{D}_\nu$, which is because the control velocity upstream of the separation

points is a suction, not a blowing (so it is of the same sign as the viscous drag sensitivity, albeit of the opposite sign as the total drag sensitivity). For the same reason, lateral suction also increases $\overline{D}_\nu$, while base bleed reduces it in a limited way. This stresses the need for a sensitivity tailored to the quantity of interest, otherwise the approach is not necessarily an improvement over trial and error design. Comparing Figs. 5(a) and 6(a), we note that the only region along the cylinder surface where pressure and viscous drag have substantial sensitivities of the same sign is at the rear surface, meaning that base bleed-like distributions are the only ones capable of reducing both $\overline{D}_p$ and $\overline{D}_\nu$. All other distributions reduce one component at the expense of the other, consistently with the results in Figs. 5(b) and 6(b).

4.3. Exact sensitivity versus self-consistent and mean flow approaches

We now turn our attention to alternative methods recently introduced to compute approximations to the mean component of the adjoint cylinder flow (which, we recall, determines the sensitivity distribution).

- a self-consistent analysis, whose solution $(\overline{\mathbf{u}}^\dagger_{\mathrm{SC}}, \overline{p}^\dagger_{\mathrm{SC}})$ takes into account that (i) the control velocity induces modifications to both the mean and the fluctuating components of the cylinder flow, and (ii) the latter feeds back on the former via the formation of Reynolds stresses [17].

- a mean flow approach, whose solution $(\overline{\mathbf{u}}^\dagger_{\mathrm{MF}}, \overline{p}^\dagger_{\mathrm{MF}})$ overlooks the modification to the fluctuating cylinder flow (or equivalently its feed back effect on the mean) [16, 18].

While we insist again that the focus of the paper is not specifically on how to derive the related adjoint equations, Appendix A sheds light on some of the key assumptions, and guides the interested reader to the original literature concerned with these topics, where in-depth technical and mathematical details are available together with extensive discussions regarding the relevance of the approximations. Suffice it to say here that both approaches strive to eliminate the need to compute and store entire time history of solutions by solving solely time-independent adjoint equations. The appendix especially emphasizes that the difference with respect to the exact sensitivity analysis is solely in the way

the interaction between the mean and fluctuating components of control-induced flow perturbation is encompassed, namely it is dismissed in the mean flow approach, or modeled by a single harmonic approximation in the self-consistent approach, hence significant differences in the computational effort. In practice, the self-consistent approach features two coupled adjoint equations, to be solved iteratively by a combination of Newton and Arnoldi methods, which can be computationally demanding albeit less demanding than going through the actual stages of the time-stepping approach. As for the mean flow approach, it relies on the resolution of a single steady adjoint equation, with the only requirement to be able to compute accurately the mean cylinder flow. The control velocity built from the self-consistent drag sensitivity shown in Fig. 7 (a) is almost identical to that using the exact, time averaged drag sensitivity, which is ascribed to the ability of the method to accurately recover the structure of the sensitivity field [17]. It thus comes as no surprise that both approaches yield the same drag reductions, both in terms of the nonlinear and linear values and regardless of the control amplitude (actually it is virtually impossible to differentiate in Fig. 7(b)). Meanwhile, the mean flow approach yields a control velocity resembling closely the exact one, especially close to the mean separation points where the sensitivity is the largest; see Fig. 8(a). The differences are in the overestimated (resp. underestimated) levels of sensitivity at the front (rear) stagnation points, and explains the discrepancy between the linear drag variations reported in Fig. 8(b). Somewhat counter-intuitively, the nonlinear variations are in closer agreement, at least up to $c_\mu \sim 0.043$ where the discrepancy is by less than 1%. Above this threshold value, the exact control velocity makes the controlled flow stable and stationary, and it has been mentioned above that it is the sensitivity of the steady drag, not that of the mean drag, that should be used for an effective control design. Owing to the subtle differences noticed in the control distributions, it however takes a larger value $c_\mu \sim 0.082$ for the approximated control to similarly quench the instability, which explains the increasing discrepancy in between these two values.

We keep in mind that the extremely high level of agreement achieved for the nonlinear variations of drag is somehow fortuitous, as it stems from the approximated velocity distribution triggering a lesser amount of nonlinearity,

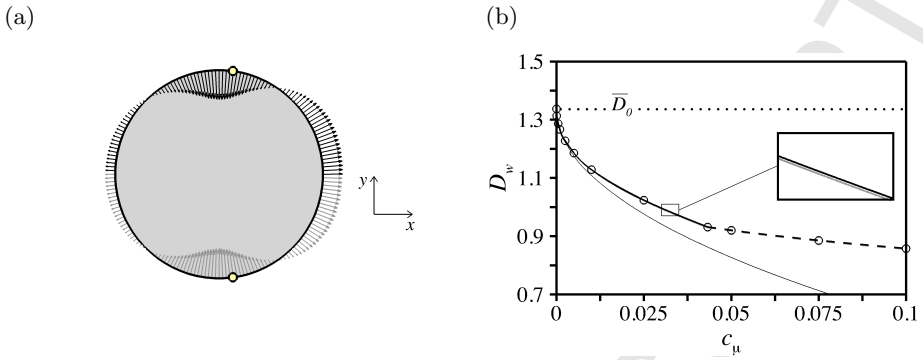

Figure 7: (a) Distribution of the wall velocity built from the self-consistent sensitivity function (upper half, black arrows) and the time averaged, exact sensitivity function (lower half, grey arrows). (b) Mean drag of the cylinder flow forced by a steady control velocity set against a model sensitivity computed by self-consistent sensitivity analysis. The thick (resp. thin) black line is the nonlinear (resp. linear) value of drag, and the solid (resp. dashed) pattern indicates time periodic (resp. steady) values. The results obtained using the time averaged, exact sensitivity are reported from Fig. 4(a) as the grey lines - $Re = 100$.

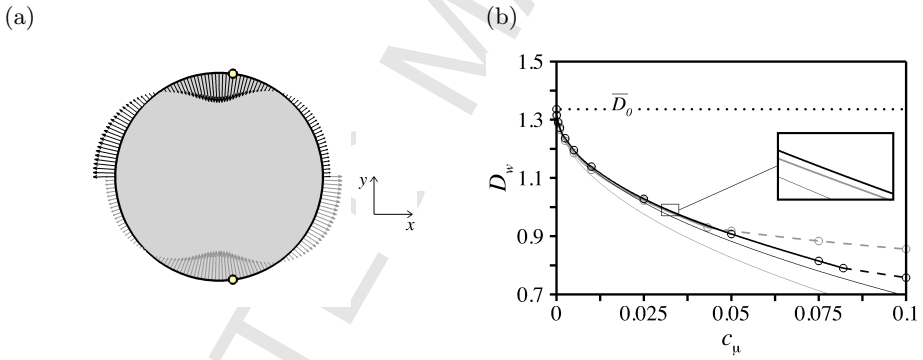

Figure 8: Same as Fig. 7 using a steady control velocity set against a model sensitivity computed by the mean flow approach.

which in turn offsets the overestimated linear variation. For all that, given the substantial differences in computational cost involved in obtaining the exact and self-consistent sensitivities [17], the mean flow approach does appear as an excellent trade-off to guide the design of near-optimal control at a reduced cost. This contrasts with the results documented in Ref. [16], where this mean flow approach is shown to capture well the flow regions where drag is most sensitive to bulk actuation, while missing substantially on secondary regions where the mean

Table 3: Details of the finite volume (FV) and finite element (FE) meshes used in the 2-D RANS analysis at $Re = 3900$.

	L_x	L_y	n_θ	n	DoF
FV	[-5, 15]	[-10, 10]	560	1.9×10^5	7.6×10^5
FE	[-5, 15]	[-10, 10]	1220	3.8×10^5	3.8×10^6

Table 4: Mean drag coefficient ($\overline{D}_0$), r.m.s. lift coefficient (L'_0), and Strouhal number (St) of the 2-D, uncontrolled cylinder flow at $Re = 3900$, together with numerical data from the literature.

Contribution	Model	$\overline{D}_0$	L'_0	St
Present	2-D RANS	1.671	1.208	0.235
Reference[a]	2-D RANS	1.642	1.184	0.243
Reference[b]	2-D LES	1.625 – 1.74	–	0.23

a: data compiled from Ref. [36].

b: data compiled from Refs. [37–39].

and fluctuating components of the solution strongly interact one with another via the formation of Reynolds stresses. Here, only the effect of wall actuation is considered. It can be postulated that accurate estimations of the control effect are obtained because the blowing velocity applied at the rear surface damps the Reynolds stresses and shifts downstream their spatial structures (as has been reported in several studies as a consequence of the increase of the formation length, i.e., the size of the region bounded by the detached shears and the eddy roll-up [32–35]), so that the main drag reduction mechanism results from mean flow modifications.

5. Towards turbulent regime

5.1. 2-D RANS modeling

We now set the Reynolds number to $Re = 3900$ to assess the applicability of a sensitivity-based control in the turbulent regime. As a first step, we perform the analysis in the frame of the 2-D Reynolds-averaged Navier–Stokes (RANS) modelling with the Spalart-Allmaras model. This simple numerical

framework can be expected to fall well short of accurately representating the finest turbulent motion, still it has proven relevant to analyze the sensitivity of turbulent wakes in fair agreement with experimental results [40, 41] because (i) the vortex-shedding period is considerably larger than the turbulent time scale (scale separation), and (ii) the primary instability triggering the onset of vortex shedding is 2-D.

The cylinder flow calculations are performed with the OpenFOAM toolbox [42], now extensively used for academic research [43–46] and industrial flow analysis [47–49]. In this study, we draw on the transient solver PimpleFOAM (which is a merging between the classical PISO and SIMPLE algorithms) and on the native implementation of the Spalart–Allmaras model packaged in official OpenFOAM releases. The governing equations are discretized by the finite volume method, with a bounded Gauss upwind scheme for the divergence terms and a Gauss linear scheme for the Laplacian terms and the gradient term. The set-up is similar to that used in Ref. [16] for the square geometry of the cylinder, for which a summary of the finite volume mesh information is provided in Table 3. We use a second-order implicit backward time advancing scheme with an adaptive time step, which yields typical values of order $\Delta t \sim 0.0015$. By doing so, we obtain an uncontrolled drag $\overline{D} = 1.671$ in good agreement with 2-D numerical data available from the literature, as shown in Table 4. We then proceed to compute the adjoint cylinder flow with the finite element solver presented in Refs. [16, 40], in which the turbulence model is implemented via user-defined closure functions. To this end, we use barycentric coordinates to interpolate the mean cylinder flow on the finite element grid whose information also is provided in Table 3. Note that the finite element grid features twice as many degrees of freedom as the finite volume grid because the inability of the finite element solver to handle element anisotropy imposes to increase the resolution at the cylinder surface to match the finite volume resolution across the viscous sublayer.

We restrict here to the sole mean flow approach, because (i) self-consistent modelling is for now restricted to laminar regimes (it remains an open issue whether it can be generalized to turbulent flows exhibiting increasing contributions from the higher-order harmonics), and (ii) it remains an open ques-

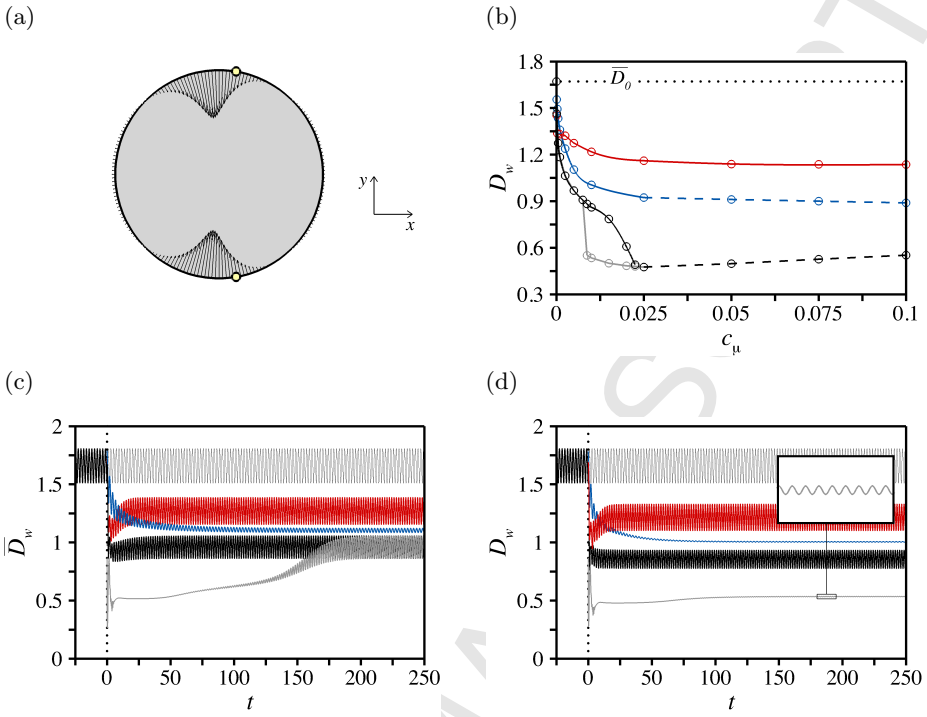

Figure 9: (a) Distribution of the wall velocity built from a model sensitivity computed by the mean flow approach in the frame of 2-D RANS modeling (i.e., both the cylinder flow and the forcing velocity are 2-D) - $Re = 3900$. (b) Mean drag of the cylinder flow forced by a steady control velocity set against a model sensitivity computed by the mean flow approach in the frame of 2-D RANS modeling. The black line (resp grey line) corresponds to forced simulations started from a developed shedding (resp. from rest), and the solid (resp. dashed) pattern indicates time periodic (resp. steady) values. (c,d) Time evolution of drag for (c) $c_\mu = 0.005$, and (d) $c_\mu = 0.015$. The fine line is the drag of the uncontrolled cylinder flow. The results obtained using base bleed (resp. lateral suction) are reported in blue (resp. in red).

tion whether a meaningful unsteady adjoint solution can be computed in high-Reynolds-number flows exhibiting chaotic features such as sensitivity with respect to initial conditions, as it is generally acknowledged that any method relying on a linearization of the unsteady Navier–Stokes equations will yield exponentially diverging solutions if the length of the adjoint simulation exceeds the predictability time scale [50, 51]. Providing an answer to this sensitive issue lies out of the scope of the present study, but we did march backwards in time the 2-D adjoint RANS equations of the drag problem and noticed such a blow

up of the adjoint solution, together with astronomically large magnitudes of sensitivity. This is in line with results reported in the 3-D flow past a circular cylinder at a Reynolds number as low as $Re = 500$ [22] and in 2-D turbulent wakes at Reynolds numbers of order 10^4 [52, 53]. The control velocity stemming from the mean flow approach, depicted in Fig. 9(a), is made up of a strong suction, distributed over the lateral sides of the cylinder with maximum upstream of the mean separation points, together with marginal blowing at the front and rear surfaces. As reported in Fig. 9(b), the latter effectively reduces drag over a large range of c_μ, while keeping a substantial advantage over base bleed and lateral suction (in this order). Note that the ability of base bleed to reduce drag is not inconsistent with the smallness of the adjoint-based velocity at the rear surface, since we recall that the sensitivity computed by the mean flow approach is only an approximation of the exact sensitivity. It however stresses the need to improve the quality of the sensitivity predictions to further cut down the cost of reducing drag. Anyhow, the present approximation achieves a minimum $\overline{D}_w = 0.48$ at $c_\mu \sim 0.025$, which represents a decrease by 71% of the uncontrolled value $\overline{D}_0 = 1.67$. This also is the critical value of c_μ allowing to quench the shedding instability, i.e., to make the flow stable and stationary. Afterwards, drag exhibits a slight increase (by up to 15% at $c_\mu = 0.1$ with respect to the minimum, still this is a decrease by 65% with respect to $\overline{D}_0$) because the high input energy tends to accumulate in the near wake. This makes the flow at the rear of the body more curved, which strengthens the pressure gradient due to the centrifugal forces and weakens the base pressure. Interestingly, the results display an hysteretic behaviour in a range of c_μ from 0.0075 to 0.0225 (those are the numerically determined values least removed from the actual hysteresis thresholds), where the efficiency is substantially better starting the control from rest (grey line) than from a developed shedding (in black). We have checked the robustness of these results by modifying the discretization scheme used to compute all cylinder flows. While this is a point for further investigation, as it clearly assesses that the control efficiency closely depends on the forcing distribution *and* the time instant at which it is applied, it is likely that the controlled steady flow undergoes a competition between several instability modes and that the adjoint-based control induce flow modifications large enough to alter the

nonlinear selection. This is supported by the fact that, when starting the control from rest, the instantaneous drags computed with $c_\mu = 0.005$ (outside the hysteresis band, Fig. 9(c)) and $c_\mu = 0.015$ (inside the hysteresis band, Fig. 9(d)) disclose identical time evolutions up to $t = 60$, but ultimately settle on distinct limit cycles.

5.2. 3-D RANS modeling

The question now being asked is what steps can be taken to raise the capability to fully 3-D turbulent flows. As a first step, we report here preliminary results obtained by computing the uncontrolled cylinder flow in the frame of 3-D RANS modeling, using periodic conditions at the span-wise, lateral boundaries. A summary of the mesh information is provided in Table 5, together with the mean flow properties in Table 6. We keep forcing in 2-D, though, so it is handy to redefine the overline as the double average over time *and* the span-wise direction, so that Eqs. (4) and (6) keep pertaining to the mean drag coefficient per unit length.

The natural extension of the mean flow approach for the double average consists in computing the sensitivity from the 2-D, time and span-wise averaged cylinder flow, as is done in Ref. [54].[3] We thus interpolate the 2-D mean flow over the same finite element grid as above, and proceed to compute the adjoint cylinder flow using the same finite element solver. By doing so, we obtain the control velocity depicted in Fig. 10(a), that closely ressembles that obtained by 2-D RANS modeling (reproduced from Fig. 9(a) in the lower half plane), except for the increased blowing velocities computed at the front surface and downstream the mean separation points. The latter is found to effectively reduce drag (for the sole comparison point at $c_\mu = 0.005$, the improvement is by 70% with respect to lateral suction, and almost twice as much, up to 135% with respect to base bleed. For the same value of the momentum coefficient, we have checked that the value $\overline{D}_w = 0.72$ obtained from the span-wise averaged

[3] It is also possible to compute a 3-D, steady sensitivity from the 3-D, time averaged cylinder flow and to deduce the 2-D sensitivity by averaging over the sole span-wise direction. The related solution comes also at a certain degree of approximation, since we recall that computing the exact sensitivity would require computing a 3-D, time-dependent sensitivity from the 3-D, time-dependent cylinder flow, and to double average over time and the span-wise direction.

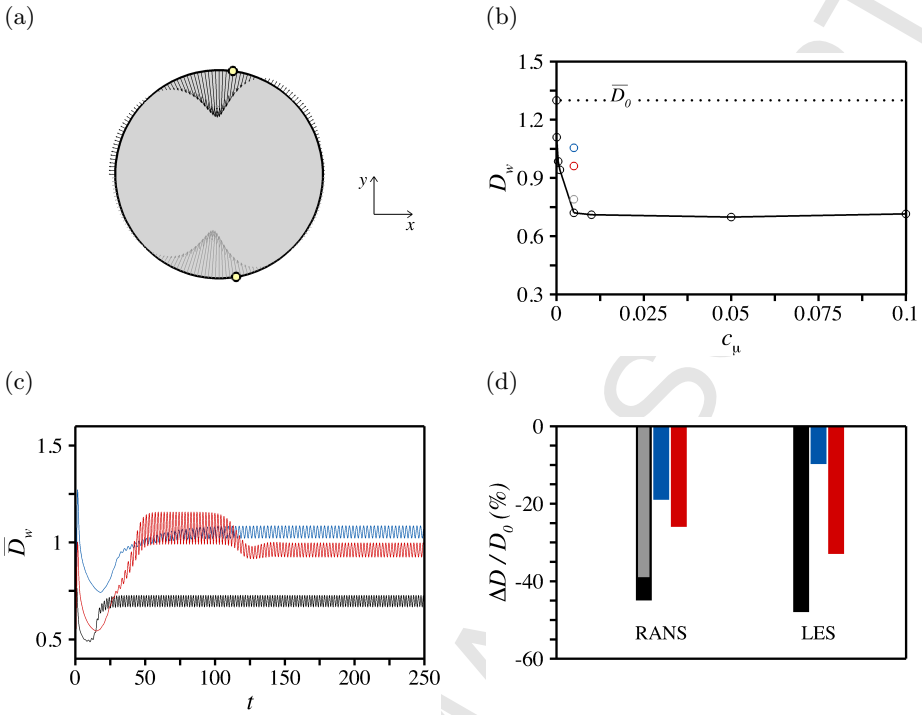

Figure 10: (a,b) Same as Fig. 9(a,b) for 2-D forcing velocities computed in the frame of 3-D RANS modeling. (c) Time evolution of drag for $c_\mu = 0.005$. (d) Comparison between RANS and LES modelling. The grey data in (b,d) denote alternative sensitivity results stemming from a 3-D RANS simulation using the sensitivity-based profile computed in the frame of 2-D RANS modeling. The results obtained using base bleed (resp. lateral suction) are reported in blue (resp. in red).

adjoint velocity is below that $\overline{D}_w = 0.79$ obtained from the purely 2-D solution (grey circle in Fig. 10(b)), which stresses the need to somehow encompass the three-dimensionality of the flow to further cut down the cost of reducing drag. Other than that, the main difference with respect to the above 2-D results lies in the inability of the control to make the flow stable and stationary, even for momentum coefficients as large as $c_\mu = 0.1$ (not shown here). Note that the efficiency of the adjoint-based control is not conditioned upon the use of RANS modeling, for instance, we have also assessed the control-induced drag variations in the frame of LES. To do so, we settle for the native implementation of the Smagorinsky subgrid scale model in OpenFOAM, corrected by a Van Driest function approaching the surface of the cylinder. We follow the guidelines

Table 5: Details of the finite volume mesh used in the 3-D RANS analysis at $Re = 3900$. L_z is the dimension of the domain in the span-wise direction.

L_x	L_y	L_z	n_θ	n	DoF
[-5, 15]	[-10, 10]	[0, 12]	240	7.4×10^6	3.7×10^7

Table 6: Mean drag coefficient ($\overline{D}_0$), r.m.s. lift coefficient (L'_0), and Strouhal number (St) of the 3-D, uncontrolled cylinder flow at $Re = 3900$, together with numerical data from the literature.

Contribution	Model	$\overline{D}_0$	L'_0	St
Present	3-D RANS	1.3	0.84	0.2
Reference[a]	3-D RANS	$1.206 - 1.373$	$0.304 - 0.846$	$0.2 - 0.215$
Present	3-D LES	1.02	0.21	0.2
Reference[b]	3-D LES	$1.016 - 1.156$	$0.25 - 0.27$	0.21

a: data compiled from Ref. [36].

b: data compiled from Refs. [20, 37, 38, 55, 56].

available in the open literature for this test case [37, 38], and use a classical cylindrical mesh with second order centered schemes for space discretization, and a second-order implicit backward time advancing scheme with a constant time step $\Delta t \sim 0.004$. This yields an uncontrolled drag $\overline{D} = 1.02$ fully consistent with the reference data available from the literature, as shown in Table 6. For a momentum coefficient $c_\mu = 0.005$, a large reduction of drag by 48% is achieved ($\overline{D}_0 = 1.02$ versus $\overline{D}_w = 0.53$), which is slightly larger than the reduction by 44% obtained in the frame of 3-RANS modeling ($\overline{D}_0 = 1.30$ versus $\overline{D}_w = 0.72$), although both approaches yield rather similar results; see the relative variations reported in Fig. 10(d).

6. Discusion

The results presented hereinabove assess the relevance of using the output of sensitivity analysis to efficiently reduce drag using 2-D control velocities distributed at the surface of a circular cylinder. They also prove feasible to design the optimal velocity at a marginal cost in the frame of the so-called mean flow

approach, whose only requisite is the knowledge of a time- and space-accurate mean flow. Promising results are especially reported in the turbulent regime, using various levels of numerical modelling to describe the small-scale turbulence.

At this stage, there are several lines of research worth pursuing to keep raising the purpose of analysis. Among them is the generalization of the method to steady, span-wise periodic actuation, which however adds a layer of complexity. This is best seen going back to the uncontrolled flow at $Re = 100$, where the leading-order variation proceeds from the second-order sensitivity, as the first-order sensitivity $\overline{\zeta}_{2D}$ is 2-D and the inner product $(\overline{\zeta}_{2D} \,|\, u_w)_\Gamma$ is thus trivially zero. While the first-order sensitivity is not necessarily zero in the most general case, the fact remains that a second-order sensitivity is likely needed to accurately predict the control-induced drag variations, and it cannot be computed with state-of-the-art adjoint method (although technical solutions have been proposed recently in the context of instability analyses [57–59]). In order to provide an insight into the stakes of this discussion, we recall that a momentum coefficient $c_\mu = 0.0175$ is needed to reduce drag by 20% at $Re = 100$ using the exact 2-D sensitivity. For comparison purposes, Ref. [20] achieves the same drag reduction using a momentum coefficient $c_\mu = 0.00175$ smaller by exactly one order of magnitude, applying a steady wall-normal lateral blowing and suction with wavelengths of order $\lambda = 4 - 5$ (this is the span-wise periodic counterpart of the empirical 2-D suction strategy considered in this study). We could not even come close with a span-wise periodic velocity built from the 2-D sensitivity, i.e., forcing with

$$u_w(\theta, z) = -\alpha \overline{\zeta}_{2D}(\theta) \cos(\frac{2\pi}{\lambda} z)\,, \tag{22}$$

for instance, Fig. 11 displays results obtained for $c_\mu = 0.00175$ and a wavelength $\lambda = 4.5$, using a doubled computational domain in the span-wise direction ($L_z = 2\lambda$) to include subharmonic perturbations. The drag reduction is by a mere 1.5%, which is comparable of the efficiency reported in Ref. [20] for wavelengths of order $\lambda \sim 2$. It remains difficult to draw a definitive conclusion, as the wavelength yielding the optimal drag reduction likely depends on the control distribution. However, this is believed to stress the need for improved theoretical frameworks to further cut down the cost of reducing drag without resorting to

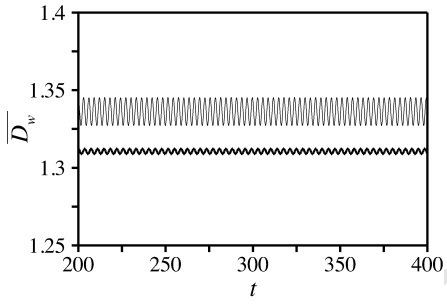

Figure 11: Time evolution of drag for a span-wise periodic, steady control velocity computed from Eq. (22) with $c_\mu = 0.00175$ and $\lambda = 4.5$ - $Re = 100$. The thick (resp. fine) line is the drag of the controlled, 3-D (uncontrolled, 2-D) cylinder flow - $Re = 100$.

exhaustive parametric studies, as there is tremendous control potential ahead. This shows in Fig. 11 through the fact that such a small value of $c_\mu = 0.00175$ suffices to produce a borderline steady controlled flow. The rms drag is about 1.26×10^{-3}, which we have checked is achieved with a purely 2-D control using a value $c_\mu \sim 0.0055$ thrice as large. This 2-D cost is obviously suboptimal as it could be substantially reduced by setting the control velocity against the sensitivity of the rms (not the mean) drag, but the same is true of the 3-D cost.

Acknowledgements

P.M. acknowledges the support of the «Investissements d'Avenir» French Government program, managed by the French National Research Agency (ANR) through the A*MIDEX grant (ANR-11-IDEX-0001-02) and the LABEX MEC project (ANR-11-LABX-0092). This work was granted access to the HPC resources of Aix–Marseille University, financed by the project Equip@Meso (ANR-10-EQPX-29-01) under the allocation amuHPC060.

A. Time-stepping analysis vs. Mean flow approach vs. Self-consistent analysis

This appendix reviews the various adjoint frameworks used in the course of this study. It is intended to shed light on some of the key assumptions, and also to serve as a guide to recently published articles about the derivation and resolution of the underlying equations. To fix a notation, we denote by an

overline and a prime superscript the (time-averaged) mean and the zero-mean fluctuation of a given quantity. Since the stress tensor is linear in the flow variables, the mean drag is entirely determined by the mean cylinder flow. The effect of the control steady velocities considered herein is not quite so simple, however, because the mean and the fluctuation are strongly coupled one to another, as established by applying Reynolds decomposition to the uncontrolled cylinder solution. In practice, there is a control-induced perturbation to the mean flow, that weighs on how the mean flow advects and produces fluctuations. This generates in turn a perturbation to the fluctuation, whose Reynolds stresses feed back on the mean to come full circle.

We now turn to the adjoint problem and restart from Eq. (9) governing the exact, time-dependent adjoint cylinder flow, recast into

$$-\partial_t \mathbf{u}^\dagger + \boldsymbol{\phi}^\dagger(\mathbf{u},\mathbf{u}^\dagger) - \boldsymbol{\nabla}\cdot\boldsymbol{\sigma}(-p^\dagger,\mathbf{u}^\dagger) = \mathbf{0}\,, \qquad \mathbf{u}^\dagger|_\Gamma = 2\mathbf{i}\,, \tag{A.1}$$

with $\boldsymbol{\phi}^\dagger(\mathbf{u},\mathbf{v}) = -\mathbf{u}\cdot\boldsymbol{\nabla}\mathbf{v} + \mathbf{v}\cdot\boldsymbol{\nabla}\mathbf{u}^T$ to ease the notation. The equations for the mean and fluctuating components are obtained by applying the Reynolds decomposition to Eq. (A.1), i.e., substituting $(\overline{\mathbf{u}}^\dagger,\overline{p}^\dagger) + (\mathbf{u}^{\dagger\prime},p^{\dagger\prime})$ for $(\mathbf{u}^\dagger,p^\dagger)$, averaging in time, then substracting from Eq. (A.1), to give

$$\boldsymbol{\phi}^\dagger(\overline{\mathbf{u}},\overline{\mathbf{u}}^\dagger) - \boldsymbol{\nabla}\cdot\boldsymbol{\sigma}(-\overline{p}^\dagger,\overline{\mathbf{u}}^\dagger) = -\overline{\boldsymbol{\phi}^\dagger(\mathbf{u}',\mathbf{u}^{\dagger\prime})}\,, \qquad \overline{\mathbf{u}}^\dagger|_\Gamma = 2\mathbf{i}\,, \tag{A.2}$$

$$\begin{aligned}-\partial_t \mathbf{u}^{\dagger\prime} + \boldsymbol{\phi}^\dagger(\overline{\mathbf{u}},\mathbf{u}^{\dagger\prime}) - \boldsymbol{\nabla}\cdot\boldsymbol{\sigma}(-p^{\dagger\prime},\mathbf{u}^{\dagger\prime}) \\ = -\boldsymbol{\phi}^\dagger(\mathbf{u}',\overline{\mathbf{u}}^\dagger) - \boldsymbol{\phi}^{\dagger\prime}(\mathbf{u}',\mathbf{u}^{\dagger\prime})\,, \qquad \mathbf{u}^{\dagger\prime}|_\Gamma = \mathbf{0}\,.\end{aligned} \tag{A.3}$$

It is thoroughly explained in Appendix A of Ref. [16] that the various terms coupling Eqs. (A.2) and (A.3) trace back directly from the Reynolds stress of the fluctuation and from the advection and production of fluctuations by the mean, that couple both components of the cylinder flow.

The mean flow approach simply dismisses the mean flow/fluctuation interaction, and therefore amounts to overlook the fluctuating adjoint cylinder flow. Equation (A.2) therefore reduces to

$$\boldsymbol{\phi}^\dagger(\overline{\mathbf{u}},\overline{\mathbf{u}}^\dagger_{\mathrm{MF}}) - \boldsymbol{\nabla}\cdot\boldsymbol{\sigma}(-\overline{p}^\dagger_{\mathrm{MF}},\overline{\mathbf{u}}^\dagger_{\mathrm{MF}}) = \mathbf{0}\,, \qquad \overline{\mathbf{u}}^\dagger_{\mathrm{MF}}|_\Gamma = 2\mathbf{i}\,, \tag{A.4}$$

and all relevant mean drag variation are obtained solving a single steady adjoint problem with the only requirement to be able to compute accurately the mean cylinder flow.

The self-consistent approach restores a model description of the interaction, based on a single harmonic approximation of the fluctuation. This reads

$$(\mathbf{u}, p) \equiv (\overline{\mathbf{u}}_{\mathrm{SC}}, \overline{p}_{\mathrm{SC}}) + 2A\Re\{(\hat{\mathbf{u}}_1, \hat{p}_1)\mathrm{e}^{\mathrm{i}\omega t}\}\,, \tag{A.5}$$

where ω is the fundamental oscillation frequency, $(\hat{\mathbf{u}}_1, \hat{p}_1)$ is the (complex) structure for the first harmonic of the fluctuation, parametrized by its (real) amplitude A, and $\Re$ denotes the real part of a complex quantity. The self-consistent analysis couples a quasi-static approximation of the instantaneous mean flow to its leading eigenmode (or instability mode), considered a relevant approximation of the first harmonic. The eigenmode feeds back onto the mean via its Reynolds stresses, which sets up a closed description of the mean flow/fluctuation interaction. For cylinder flows whose nonlinearity involves little production of higher harmonics [60, 61], the self-consistent analysis aims at determining the amplitude A yielding a neutrally stable mean flow, at which point the fundamental frequency is given by the leading eigenfrequency. This is examined in greater detail in Refs. [62, 63], together with numerical methods for computing the self-consistent cylinder flow by a combination of Newton and Arnoldi methods. It is especially made clear that the self-consistent mean flow $(\overline{\mathbf{u}}_{\mathrm{SC}}, \overline{p}_{\mathrm{SC}})$ is not a given but an output (hence the specific notation) because it must be balanced by the Reynolds stresses of the leading eigenmode, while a DNS mean flow encompasses the effect of all harmonics. The adjoint solution is similarly expanded as

$$(\mathbf{u}^\dagger, p^\dagger) \equiv (\overline{\mathbf{u}}^\dagger_{\mathrm{SC}}, \overline{p}^\dagger_{\mathrm{SC}}) + 2\Re\{(\hat{\mathbf{u}}^\dagger_1, \hat{p}^\dagger_1)\mathrm{e}^{\mathrm{i}\omega t}\}\,, \tag{A.6}$$

and the various components come as the coupled solutions to system

$$\boldsymbol{\phi}^\dagger(\overline{\mathbf{u}}_{\mathrm{SC}}, \overline{\mathbf{u}}^\dagger_{\mathrm{SC}}) - \boldsymbol{\nabla}\cdot\boldsymbol{\sigma}(-\overline{p}^\dagger_{\mathrm{SC}}, \overline{\mathbf{u}}^\dagger_{\mathrm{SC}}) = -2A\Re\{\boldsymbol{\phi}^\dagger(\hat{\mathbf{u}}_1, \hat{\mathbf{u}}_1^{\dagger *})\}\,, \quad \overline{\mathbf{u}}^\dagger_{\mathrm{SC}}|_\Gamma = 2\mathbf{i}\,, \tag{A.7}$$

$$-\mathrm{i}\omega\hat{\mathbf{u}}^\dagger_1 + \boldsymbol{\phi}^\dagger(\overline{\mathbf{u}}_{\mathrm{SC}}, \hat{\mathbf{u}}^\dagger_1) - \boldsymbol{\nabla}\cdot\boldsymbol{\sigma}(-\hat{p}^\dagger_1, \hat{\mathbf{u}}^\dagger_1) = -A\boldsymbol{\phi}^\dagger(\hat{\mathbf{u}}_1, \overline{\mathbf{u}}_{\mathrm{SC}})\,, \quad \hat{\mathbf{u}}^\dagger_1|_\Gamma = \mathbf{0}\,, \tag{A.8}$$

$$(\overline{\mathbf{u}}^\dagger_{\mathrm{SC}}\,|\,\boldsymbol{\phi}(\hat{\mathbf{u}}_1, \hat{\mathbf{u}}_1{}^*))_\Omega = 0\,, \tag{A.9}$$

$$\alpha^\dagger + 2A(\hat{\mathbf{u}}^\dagger_1\,|\,\hat{\mathbf{u}}_1)_\Omega = 0\,, \tag{A.10}$$

where $\alpha^\dagger$ is a specific adjoint variable meant to fulfill the neutral stability condition, we note $\boldsymbol{\phi}(\mathbf{u}, \mathbf{v}) = \mathbf{u}\cdot\boldsymbol{\nabla}\mathbf{v} + \mathbf{v}\cdot\boldsymbol{\nabla}\mathbf{u}$, and the right-hand sides of Eqs. (A.7) and (A.8) turn to be the single harmonic approximations of those in Eqs. (A.2) and (A.3). The above equations are analytically derived in Appendix A of

Ref. [17], and the resolution is performed in Appendix B using a low cost sequential, iterative algorithm. This is because all equations are independent of time, which eliminates the need to store entire time history of solutions, and tremendously reduces the computational cost.

References

[1] M. Gad-el Hak, Modern developments in flow control, Appl. Mech. Rev. 49 (7) (1996) 365–379.

[2] J. Lumley, P. Blossey, Control of turbulence, Annu. Rev. Fluid Mech. 30 (1998) 311–327.

[3] A. Glezer, M. Amitay, Synthetic jets, Annu. Rev. Fluid Mech. 34 (1) (2002) 503–529.

[4] S. S. Collis, R. D. Joslin, A. Seifert, V. Theofilis, Issues in active flow control: theory, control, simulation, and experiment, Prog. Aerosp. Sci. 40 (2004) 237–289.

[5] J. Kim, T. R. Bewley, A linear systems approach to flow control, Annu. Rev. Fluid Mech. 39 (2007) 383–417.

[6] H. Choi, W.-P. Jeon, J. Kim, Control of flow over a bluff body, Annu. Rev. Fluid Mech. 40 (2008) 113–139.

[7] T. C. Corke, C. L. Enloe, S. P. Wilkinson, Dielectric barrier discharge plasma actuators for flow control, Annu. Rev. Fluid Mech. 42 (2010) 505–529.

[8] L. N. Cattafesta, M. Sheplak, Actuators for active flow control, Annu. Rev. Fluid Mech. 43 (2011) 247–272.

[9] A. Seifert, Boundary layer separation control: Experimental perspective and modeling outlook, Annu. Rev. Fluid Mech. 50 (2018) null.

[10] D. C. Hill, A theoretical approach for analyzing the restabilization of wakes, Technical memorandum NASA-TM-103858, NASA (1992).

[11] M. D. Gunzburger, Perspectives in flow control and optimization, SIAM, Philadelphia, 2002.

[12] F. Giannetti, P. Luchini, Structural sensitivity of the first instability of the cylinder wake, J. Fluid Mech. 581 (2007) 167–197.

[13] O. Marquet, D. Sipp, L. Jacquin, Sensitivity analysis and passive control of cylinder flow, J. Fluid Mech. 615 (2008) 221–252.

[14] J. O. Pralits, L. Brandt, F. Giannetti, Instability and sensitivity of the flow around a rotating circular cylinder, J. Fluid Mech. 650 (2010) 513–536.

[15] D. Sipp, O. Marquet, P. Meliga, A. Barbagallo, Dynamics and control of global instabilities in open-flows: a linearized approach, Appl. Mech. Rev. 63 (2010) 030801.

[16] P. Meliga, E. Boujo, G. Pujals, F. Gallaire, Sensitivity of aerodynamic forces in laminar and turbulent flow past a square cylinder, Phys. Fluids 26 (2014) 104101.

[17] P. Meliga, Computing the sensitivity of drag and lift in flow past a circular cylinder: time-stepping vs. self-consistent analysis, Phys. Rev. Fluids 2 (2017) 073905.

[18] X. Mao, Sensitivity of forces to wall transpiration in flow past an aerofoil, Proc. R. Soc. A 471 (2015) 20150618.

[19] M. M. Zdravkovich, Review and classification of various aerodynamic and hydrodynamic means for suppressing vortex shedding, J. Wind Eng. Ind. Aerodyn. 7 (2) (1981) 145–189.

[20] J. Kim, H. Choi, Distributed forcing of flow over a circular cylinder, Phys. Fluids 17 (3) (2005) 033103.

[21] M. Amitay, A. Glezer, Role of actuation frequency in controlled flow reattachment over a stalled airfoil, AIAA J. 40 (2002) 209–216.

[22] Q. Wang, J.-H. Gao, The drag-adjoint field of a circular cylinder wake at reynolds numbers 20, 100 and 500, J. Fluid Mech. 730 (2013) 145–161.

[23] J. Park, K. Kwon, H. Choi, Numerical solutions of flow past a circular cylinder at reynolds numbers up to 160, KSME Int. J. 12 (1998) 1200–1205.

[24] S. Mittal, Excitation of shear layer instability in flow past a cylinder at low Reynolds number, Int. J. Numer. Meth. Fl. 49 (10) (2005) 1147–1167.

[25] Y. Wang, G. Haller, A. Banaszuk, G. Tadmor, Closed-loop Lagrangian separation control in a bluff body shear flow model, Phys. Fluids 15 (8) (2003) 2251–2266.

[26] P. Meliga, E. Boujo, F. Gallaire, A self-consistent formulation for the sensitivity analysis of finite amplitude vortex shedding in the cylinder wake, J. Fluid Mech. 800 (2016) 327–357.

[27] W. Bearman, The effect of base bleed on the flow behind a two-dimensional model with a blunt trailing edge, Aeronaut. Q. 18 (1967) 207–224.

[28] M. Schumm, E. Berger, P. A. Monkewitz, Self-excited oscillations in the wake of two-dimensional bluff bodies and their control, J. Fluid Mech. 271 (1994) 17–53.

[29] Y. Delaunay, L. Kaiktsis, Control of circular cylinder wakes using base mass transpiration, Phys. Fluids 13 (2001) 3285–3302.

[30] C. Castro, C. Lozano, F. Palacios, E. Zuazua, Systematic continuous adjoint approach to viscous aerodynamic design on unstructured grids, AIAA J. 45 (9) (2007) 2125–2139.

[31] E. Boujo, An adjoint-based approach to the optimal control of separated flows, Ph.D. thesis, École Polytechnique Fédérale de Lausanne (2014).

[32] B. Thiria, J. E. Wesfreid, Stability properties of forced wakes, J. Fluid Mech. 579 (2007) 137–161.

[33] V. Parezanović, O. Cadot, The impact of a local perturbation on global properties of a turbulent wake, Phys. Fluids 21 (7) (2009) 071701.

[34] B. Thiria, O. Cadot, J.-F. Beaudoin, Passive drag control of a blunt trailing edge cylinder, J. Fluid Struct. 25 (4) (2009) 766–776.

[35] V. Parezanović, O. Cadot, Experimental sensitivity analysis of the global properties of a two-dimensional turbulent wake, J. Fluid Mech. 693 (2012) 115–149.

[36] F. Pereira, G. Vaz, L. Eça, Flow past a circular cylinder: a comparison between rans and hybrid turbulence models for a low Reynolds number, OMAE 2015-41235.

[37] M. Breuer, Large eddy simulation of the subcritical flow past a circular cylinder: Numerical and modeling aspects, Int. J. Numer. Meth. Fl. 28 (1998) 1281–1302.

[38] A. G. Kravchenko, P. Moin, Numerical studies of flows over a circular cylinder at $Re_d = 3900$, Phys. Fluids 12 (2000) 403–417.

[39] S. P. Singh, S. Mittal, Flow past a cylinder: shear layer instability and drag crisis, Int. J. Numer. Meth. Fl. 47 (2005) 75–98.

[40] P. Meliga, G. Pujals, E. Serre, Sensitivity of 2-D turbulent flow past a D-shaped cylinder using global stability, Phys. Fluids 24 (2012) 061701.

[41] P. Meliga, O. Cadot, E. Serre, Experimental and theoretical sensitivity analysis of turbulent flow past a square cylinder, Flow Turbul. Combust. 97 (2016) 987–1015.

[42] Source code and official documentation available at http://www.openfoam.org.

[43] G. R. Tabor, M. H. Baba-Ahmadi, Inlet conditions for large eddy simulation: A review, Comp. Fluids 39 (2010) 553–567.

[44] M. Meldi, M. V. Salvetti, P. Sagaut, Quantification of errors in large-eddy simulations of a spatially evolving mixing layer using polynomial chaos, Phys. Fluids 24 (2012) 035101.

[45] D. A. Lysenko, I. S. Ertesvåg, K. E. Rian, Modeling of turbulent separated flows using OpenFOAM, Comp. Fluids 80 (2013) 408–422.

[46] E. M. J. Komen, A. Shams, L. Camilo, B. Koren, Quasi-DNS capabilities of OpenFOAM for different mesh types, Comp. Fluids 96 (2014) 87–104.

[47] L. Gao, J. Xu, G. Gao, Numerical simulation of turbulent flow past airfoils on OpenFOAM, Comp. Fluids 31 (2012) 756–761.

[48] F. Flores, R. Garreaud, R. C. Muñoz, CFD simulations of turbulent buoyant atmospheric flows over complex geometry: Solver development in OpenFOAM, Comp. Fluids 82 (2013) 1–13.

[49] B. Selma, M. Désilets, P. Proulx, Optimization of an industrial heat exchanger using an open-source CFD code, Appl. Therm. Eng. 69 (2014) 241–250.

[50] D. J. Lea, A. Myles, T. W. N. Haines, Sensitivity analysis of the climate of a chaotic system, Tellus A 52 (2000) 523–532.

[51] A. Köhl, J. Willebrand, An adjoint method for the assimilation of statistical characteristics into eddy-resolving ocean models, Tellus A 54 (2002) 406–425.

[52] T. J. Barth, On the role of error and uncertainty in the numerical simulation of complex fluid flows, presented at the 2010 SIAM Annual Meeting, SIAM, Philadelphia (2010).

[53] M. Nazarov, J. Hoffman, On the stability of the dual problem for high reynolds number flow past a circular cylinder in two dimensions, SIAM J. Sci. Comput. 34 (2012) A1905–A1924.

[54] C. Mettot, D. Sipp, H. Bézard, Quasi-laminar stability and sensitivity analyses for turbulent flows: Prediction of low-frequency unsteadiness and passive control, Phys. Fluids 26 (4) (2014) 045112.

[55] F. Tremblay, Direct and large eddy simulation of fow around a circular cylinder at subcritical Reynolds numbers, Ph.D. thesis, Technischen Universität München (2002).

[56] H. Naito, K. Fukagata, Numerical simulation of flow around a circular cylinder having porous surface, Phys. Fluids 24 (2012) 117102.

[57] O. Tammisola, F. Giannetti, V. Citro, M. P. Juniper, Second-order perturbation of global modes and implications for spanwise wavy actuation, J. Fluid Mech. 755 (2014) 314–335.

[58] E. Boujo, A. Fani, F. Gallaire, Second-order sensitivity of parallel shear flows and optimal spanwise-periodic flow modifications, J. Fluid Mech. 782 (2015) 491–514.

[59] O. Tammisola, Optimal wavy surface to suppress vortex shedding using second-order sensitivity to shape changes, Eur. J. Mech. B-Fluid 62 (2016) 139–148.

[60] J. Dušek, P. Le Gal, P. Fraunié, A numerical and theoretical study of the first Hopf bifurcation in a cylinder wake, J. Fluid Mech. 264 (1994) 59–80.

[61] B. Protas, J. E. Wesfreid, Drag force in the open-loop control of the cylinder wake in the laminar regime, Phys. Fluids 14 (2002) 810–826.

[62] V. Mantič-Lugo, C. Arratia, F. Gallaire, Self-consistent mean flow description of the nonlinear saturation of the vortex shedding in the cylinder wake, Phys. Rev. Lett. 113 (2014) 084501.

[63] V. Mantič-Lugo, C. Arratia, F. Gallaire, A self-consistent model for the saturation dynamics of the vortex shedding around the mean flow in the unstable cylinder wake, Phys. Fluids 27 (2015) 074103.